

Elevated foehn exacerbates surface ozone pollution in summer Beijing

Zhiheng Liao¹, Jing Xu¹, Ju Li¹, Liyan Zhou¹, Chao Liu¹, Lin Wu², Zhiqiang Ma¹

¹Institute of Urban Meteorology, China Meteorological Administration, Beijing, China;

²Huairou Meteorological Office of Beijing, Beijing, China.

Correspondence: Z. Liao (zhliao@ium.cn) and Z. Ma (zqma@ium.cn)

Abstract: While several studies have evaluated the impact of shallow foehn on air pollution, the effects of elevated foehn on O₃ pollution remain poorly understood. Here, we investigate the role of elevated foehn in summer O₃ pollution in Beijing through detailed case analysis and a long-term climatological evaluation. The case study reveals that elevated foehn exacerbates next-day O₃ pollution through three primary mechanisms: first, by increasing boundary layer temperature, thereby enhancing photochemical O₃ formation; second, by reducing the residual/boundary layer height, thereby inhibiting vertical diffusion of pollutants; and third, by slowing boundary layer winds, thereby suppressing horizontal dispersion. A ten-year climatological evaluation of 54 identified elevated foehn events strongly supports these mechanisms. On average, these events led to a post-foehn afternoon boundary layer temperature increase exceeding 3°C, an afternoon boundary layer height reduction of more than 100 m, and a decrease in afternoon boundary layer wind speed of more than 1.0 m s⁻¹ compared to the pre-foehn days. Consequently, 87% of elevated foehn events were associated with a worsening of O₃ pollution. Post-foehn daily maximum 8-hour average O₃ concentrations frequently surpassed the national pollution threshold (160 µg m⁻³), with an average increase of 20%–60% (varying by site and higher in urban areas) compared to preceding days. These results demonstrate a robust and deterministic exacerbating effect of elevated foehn on surface O₃ pollution, suggesting that elevated foehn can serve as a reliable meteorological precursor for O₃ pollution warnings in summer Beijing.

Keywords: elevated foehn, atmospheric boundary layer, residual layer warming, ozone pollution, Beijing

1. Introduction

Foehn is a phenomenon of downslope winds with significant warming on the mountain leeward side (Elvidge and Renfrew, 2016). It has been observed among many large mountains in the world, including the Alpine Mountains (Miltenberger et al., 2016; Seibert et al., 2000), Rocky Mountains (Kerr, 1986), Appalachian Mountains (Gaffin, 2002, 2009), Taihang Mountains (Li et al., 2020a; Li et al., 2025), and Tianshan Mountains (Li et al., 2015; Li et al., 2020b). The societal and economic impacts of foehn winds are wide-ranging and well-documented, encompassing enhanced fire risks, extreme heat exposure, impacts on air quality, beneficial impacts on agriculture, and direct wind-driven damage to infrastructure. Given these multifaceted impacts, foehn has long been a subject of sustained scholarly interest across diverse disciplines.

Scientific research into the effect of foehn on air pollution began in Europe in the late nineteenth century, primarily to explain elevated ozone (O₃) levels in the Alpine regions during foehn events (Baumann et al., 2001; Campana et al., 2005; Seibert et al., 2000). Early European studies identified that the initial rise in O₃ concentration was caused by the advection of residual-layer air masses from source regions such as the Po Basin. Later on, O₃ levels in the foehn-affected area were found to be influenced by regional-scale advection from the lower free troposphere or even the stratosphere. Collectively, these studies emphasized the transport role of foehn in

45 influencing O₃ air quality in the relatively clean valleys of Alps. In contrast, research in China has commonly
46 demonstrated a “clearance effect” of foehn on air pollution in highly-polluted cities (Li et al., 2020a; Li et al., 2025;
47 Yang et al., 2018). For example, Yang et al. (2018) reported a case in Shijiazhuang where foehn led to rapidly
48 improved horizontal visibility, decreased aerosol concentration, and weakened haze intensity. Similarly, a six-year
49 statistical study by Li et al. (2025) found that 60.4 % of foehn events were associated with a subsequent decrease in
50 fine particulate matter (PM_{2.5}) concentrations in Beijing. This clearance effect is attributed to the origin of the foehn
51 winds, which typically transport cleaner air from the less polluted western, northwestern and northern mountain
52 areas of the Hebei–Beijing region into more polluted plains.

53

54 These abovementioned studies, conducted in both Europe and China, primarily examine the foehn effect on air
55 pollution mainly from a dynamical (transport) perspective. Furthermore, the foehn cases selected in these studies
56 are generally confined to shallow foehns, identifying using near-surface meteorological observations. Crucially,
57 however, the defining feature of foehn is the associated warming (Elvidge and Renfrew, 2016). This warming
58 inevitably alters the vertical thermal structure—and thus the atmospheric stability—which directly governs the
59 capacity for vertical diffusion of air pollutants (Liao et al., 2018; Stull, 1988). Therefore, the vertical extent of the
60 foehn (shallow or elevated) critically determines its impact on atmospheric stability: shallow foehn tends to
61 enhance near-surface instability, while elevated foehn can strengthen stability within or above the boundary layer.
62 From this thermodynamic perspective, elevated foehn likely possesses a greater pollution potential than its shallow
63 counterpart. Despite this reasoning, to the best of our knowledge, only one study—Li et al. (2015) in Urumqi, a city
64 adjacent to Tianshan Mountains—has explicitly investigated the impact of an elevated foehn on air pollution from a
65 thermodynamic viewpoint. That study revealed that an elevated southeasterly foehn layer between 480 and 2100 m
66 created a very stable boundary layer structure, which suppressed vertical mixing and led to severe haze pollution
67 episodes. Recent studies on PM_{2.5} pollution in Beijing (Li et al., 2020a; Li et al., 2025) have speculated that
68 post-foehn pollution exacerbation might be driven by a mechanism similar to the elevated foehn process observed
69 in Urumqi (Li et al., 2015). However, the existence and role of such an elevated foehn mechanism have not yet
70 been observationally confirmed for Beijing.

71

72 Beijing, the capital of China, faces significant challenges in terms of air pollution. Particularly in recent summers,
73 O₃ has surpassed PM_{2.5} as the most important air pollutant, arousing widespread attention (Liao et al., 2023; Zong
74 et al., 2023). The city’s location on the plains adjacent to the Taihang Mountains to the west and the Yan Mountains
75 to the north makes it particularly susceptible to foehn winds (Xu et al., 2026). Luo et al. (2020) documented an
76 intensive foehn warming event in Beijing where nocturnal air temperatures increased by over 10°C per hour.
77 Utilizing data from a density automatic weather station network, Li et al. (2025) developed a foehn identification
78 method and reported an annual average of 56.5 foehn days in Beijing. As noted earlier, their statistical analysis
79 suggests a higher probability of PM_{2.5} pollution alleviation (60.4 %) rather than pollution exacerbation (39.6 %)
80 following foehn events in Beijing. Importantly, because their identification method only relies on near-surface
81 observations, the detected events are predominantly shallow foehns. This methodological focus may obscure the
82 distinct air pollution effects potentially caused by elevated foehns. Therefore, determining whether elevated foehn
83 induces a more deterministic—and likely adverse—pollution effects is a critical unanswered question. The answer
84 has practical importance, as it would inform whether elevated foehn can serve as a reliable precursor indicator for
85 air pollution warnings, thereby improving mitigation efforts in Beijing and other leeside cities.

86

87 To address this knowledge gap, our team deployed two O₃ lidars at an urban (Guanxiangtai, GXT) and a rural
88 (Shangdianzi, SDZ) station in Beijing in late July 2024. This coordinated dual-station lidar setup is particularly

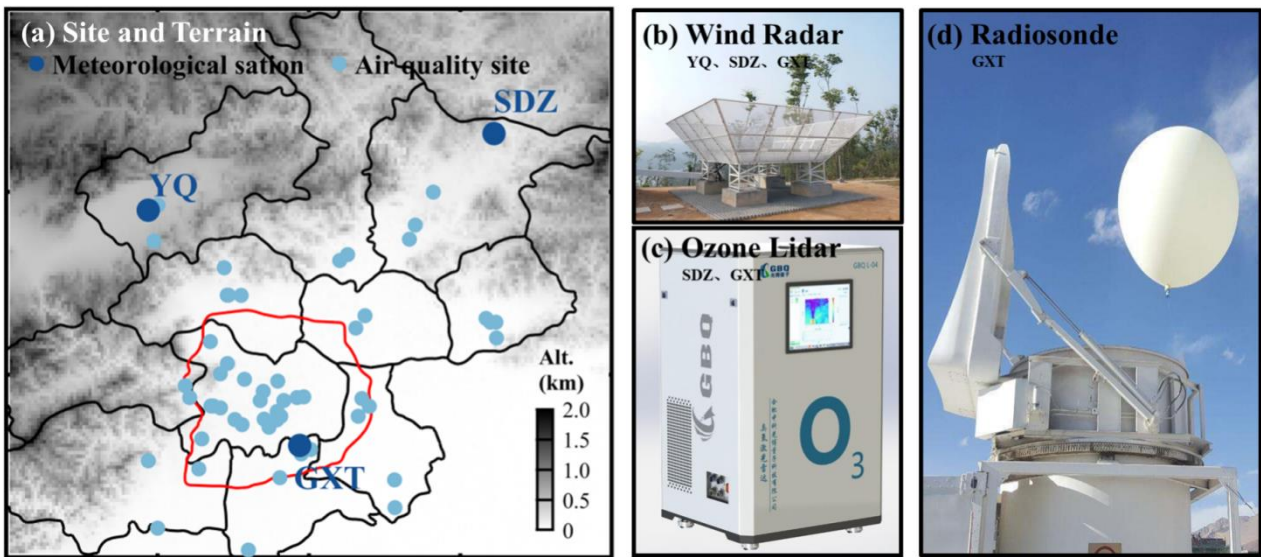
89 suited to capturing the three-dimensional characteristics and mechanisms of boundary layer O₃ evolution under the
90 influence of elevated foehn. One month after deployment (27–31 August), we observed an O₃ pollution episode
91 associated with an elevated foehn. In this study, we conducted a detailed analysis of this event by integrating data
92 from the new lidar system with co-located remote sensing meteorological observations. We supplement this case
93 study with a climatological evaluation using a decade (2015–2024) of routine observations. Our overarching aim is
94 to elucidate the specific role of elevated foehn in driving summer O₃ pollution in Beijing.

95

96 2. Data and method

97 2.1. Observational data

98 Figure 1 shows the observation network and instruments. The network comprises 3 meteorological stations and
99 46 surface O₃ monitoring sites. Among the O₃ sites, 45 are air quality stations operated by the Beijing Municipal
100 Ecological and Environmental Monitoring Center, and one is the Shangdianzi (SDZ) atmospheric background
101 station managed by the Beijing Meteorological Bureau. Two differential absorption O₃ lidars (Hefei GBQ
102 Technology Company) were deployed at the GXT (urban) and SDZ (rural) stations, respectively. These lidars
103 measured O₃ profiles with a 5-minute resolution up to an altitude of 3.0 km. In addition, radar wind profilers at
104 GXT, SDZ, as well as Yanqing (YQ) provided continuous wind profiles at 6-minute resolution. Routine
105 meteorological radiosondes launched from the GXT station provided high-vertical-resolution (~10 m) profiles of
106 temperature, relative humidity, wind speed, and wind direction three times daily (08:00, 14:00, and 20:00 BJT) in
107 summer.



108

109 **Figure 1.** Site distribution of surface ozone and meteorological measurements, and ground-based remote sensing
110 instruments used in this study. In (a), dark blue dots denote the GXT, SDZ, and YQ meteorological stations; light
111 blue dots represent the surface ozone observation sites. Panels (b), (c), and (d) show the radar wind profilers at YQ,
112 SDZ, and GXT, ozone lidars at SDZ and GXT, and routine radiosonde instrument at GXT, respectively.

113

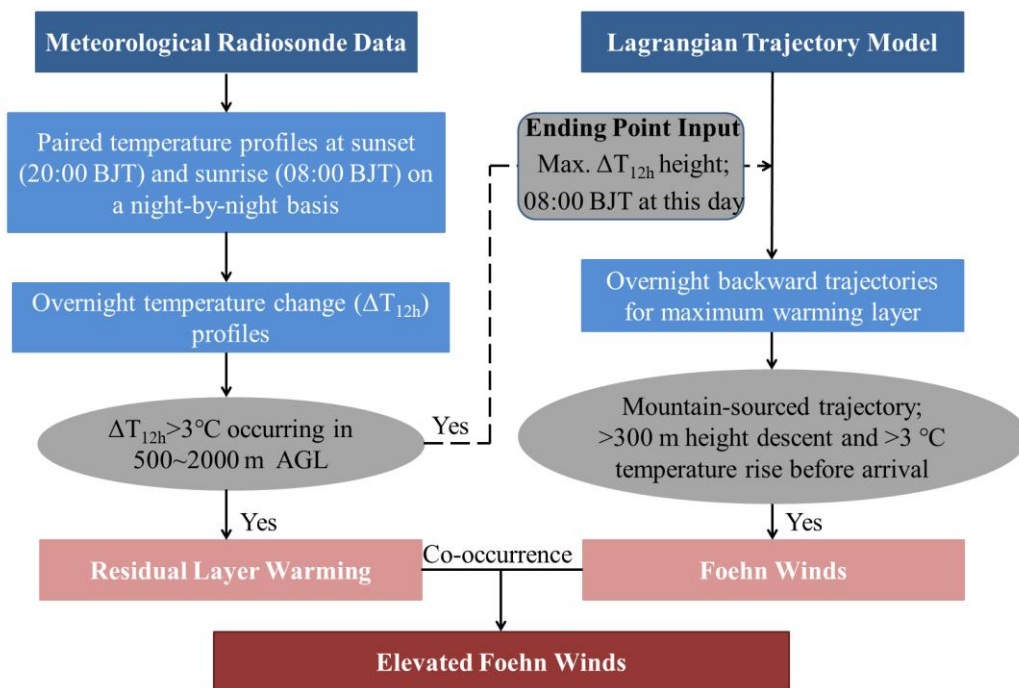
114 To validate the lidar O₃ observations, we compared the lidar-derived O₃ concentration at 300 m height (the
115 lowest reliable altitude above the instrument's blind zone) with surface measurements. As no surface O₃ data were
116 available at the GXT site, we used measurements from the nearest air quality monitoring station (~2 km away). The
117 validation results demonstrated a strong correlation between the lidar-based and surface-based O₃ concentrations
118 ($R^2 = 0.69$ at GXT and $R^2 = 0.56$ at SDZ), confirming the reliability of the O₃ lidar data (Fig. S1). To construct

119 complete vertical profiles for calculating O₃ transport flux, we used linear interpolation between the surface O₃
 120 measurement and the validated lidar observation at 300 m to fill the blind zone. A similar procedure was applied to
 121 patch the blind zone (below 150 m) of the radar wind profiler data, where winds were interpolated between the
 122 surface wind observation and the lowest valid radar measurement at 150 m.

123

124 2.2. Identification of elevated foehn

125 To date, no established method exists for identifying elevated foehn. For the purpose of climatological evaluation,
 126 we develop a framework (Fig. 2) to identify elevated foehn events based on the combination of meteorological
 127 radiosonde data and a Lagrangian trajectory model. First, we calculated overnight temperature change (ΔT_{12h})
 128 profiles by subtracting the radiosonde temperature profiles at 20:00 BJT (sunset) from the profiles at 08:00 BJT the
 129 following day (sunrise) on a night-by-night basis (i.e., $\Delta T_{12h}=T_{08}-T_{20}$). A residual layer warming event was
 130 identified when $\Delta T_{12h}>3^{\circ}\text{C}$ occurred within 500-2000 m AGL layer. This threshold is also commonly used to
 131 identify ground-based foehn elsewhere (Kirchgaessner et al., 2021; Steinhoff et al., 2014). Finally, we examined the
 132 backward trajectory properties (including geographic origin, height change, and temperature change) of the air
 133 mass at the identified maximum warming height (i.e., the height of maximum ΔT_{12h}) using a Lagrangian trajectory
 134 model (Miltenberger et al., 2016). If the 12-h backward trajectory originated from the mountains (azimuth of 250–
 135 360° or 0–45°, following Li et al. (2025)), and if the trajectory descended more than 300 m accompanied by a
 136 temperature increase exceeding 3 °C before arriving in Beijing, we attribute the identified warming case to an
 137 elevated foehn event.



138

139 **Figure 2.** Flowchart for identifying elevated foehn based on the combination of meteorological radiosonde data and
 140 a Lagrangian trajectory model.

141

142 2.3. Supporting calculations and model simulations

143 The boundary layer structure during a diurnal cycle can be classified into three regimes: convective boundary
 144 layer (CBL), stable boundary layer (SBL), and residual layer (RL) (Stull, 1988). We determined the boundary layer
 145 height based on high-resolution radiosonde profiles from the GXT station. Following Liu and Liang (2010), the
 146 height of the CBL (CBLH, at 14:00 BJT) was determined at the base of the overlying temperature inversion

147 capping the convective thermals. The height of the SBL (SBLH, at 20:00 and 08:00 BJT) was determined at the top
148 of the underlying temperature inversion, where turbulence nearly ceases. At the morning transition (08:00 BJT),
149 emerging solar radiation gradually erodes the near-surface part of the SBL; thus, the SBLH at this time was
150 determined at the top of the residual underlying temperature inversion. The RL is disconnected from the ground by
151 the underlying SBL but retains the atmospheric state of the former CBL. Its height (RLH) was therefore determined
152 at the base of the overlying temperature inversion at the evening or morning transition (20:00 and 08:00 BJT). For
153 temperature profiles showing no significant overlying inversion, the CHLH and RLH were determined using a
154 multi-variable integrated method proposed by Wang and Wang (2014).

155
156 To analyze O₃ transport in Beijing, we calculated the O₃ transport flux (TF) using collocated wind and O₃ profiles
157 from the GXT and SDZ sites. The transport flux (TF, mg m⁻² s⁻¹), representing the mass flow per unit
158 cross-sectional area per unit time, is determined by the wind speed and the O₃ concentration. The TF at a certain
159 height and direction is calculated as follow:

$$160 \quad TF = C \times WS \times \cos \left[(WD - B) \times \frac{\pi}{180} \right]$$

161 where C represents the O₃ concentration (unit: μg m⁻³), WS denotes the horizontal wind speed (unit: m s⁻¹), WD
162 denotes the horizontal wind direction and B is the azimuth from the start station to the end station. In this study, we
163 calculated O₃ transport flux in the direction from GXT to SDZ. Therefore, positive TF indicates northeastward
164 transport, and negative TF indicates southwestward transport.

165
166 We used the Hybrid Single-Particle Lagrangian Integrated Trajectory (HYSPPLIT) model (Stein et al., 2015) to
167 trace the origin and history of the air masses associated with the maximum residual layer warming in Beijing. In
168 addition to HYSPPLIT, we employed the Weather Research and Forecasting model with Chemistry (WRF-Chem,
169 version 4.2.1) to simulate O₃ concentrations and meteorological fields. The WRF-Chem model accounts for key
170 atmospheric processes, including emissions, deposition, advection, diffusion, gas-phase chemistry, and aerosol
171 chemistry (Grell et al., 2005). Our simulation domain encompassed most of China, centered at (105.5°E, 37.5°N),
172 with a horizontal grid spacing of 9 km. The meteorological initial and boundary conditions were derived from the
173 National Centers for Environmental Prediction (NCEP) Final Operational Global Analysis data. For emissions, we
174 utilized the Model of Emissions of Gases and Aerosols from Nature (MEGAN) (Guenther et al., 2006) and the
175 Multi-resolution Emission Inventory for China (MEIC) (Zhang et al., 2009), with the latter updated to a 0.1° × 0.1°
176 resolution for 2019 (MEIC-2019; <http://www.meicmodel.org>). The detailed model configuration follows Xu et al.
177 (2024). The WRF-Chem simulation demonstrated a reasonable agreement with observed surface O₃ concentrations
178 during the studied pollution episode (R² = 0.51 at GXT and R² = 0.44 at SDZ; Fig. S2).

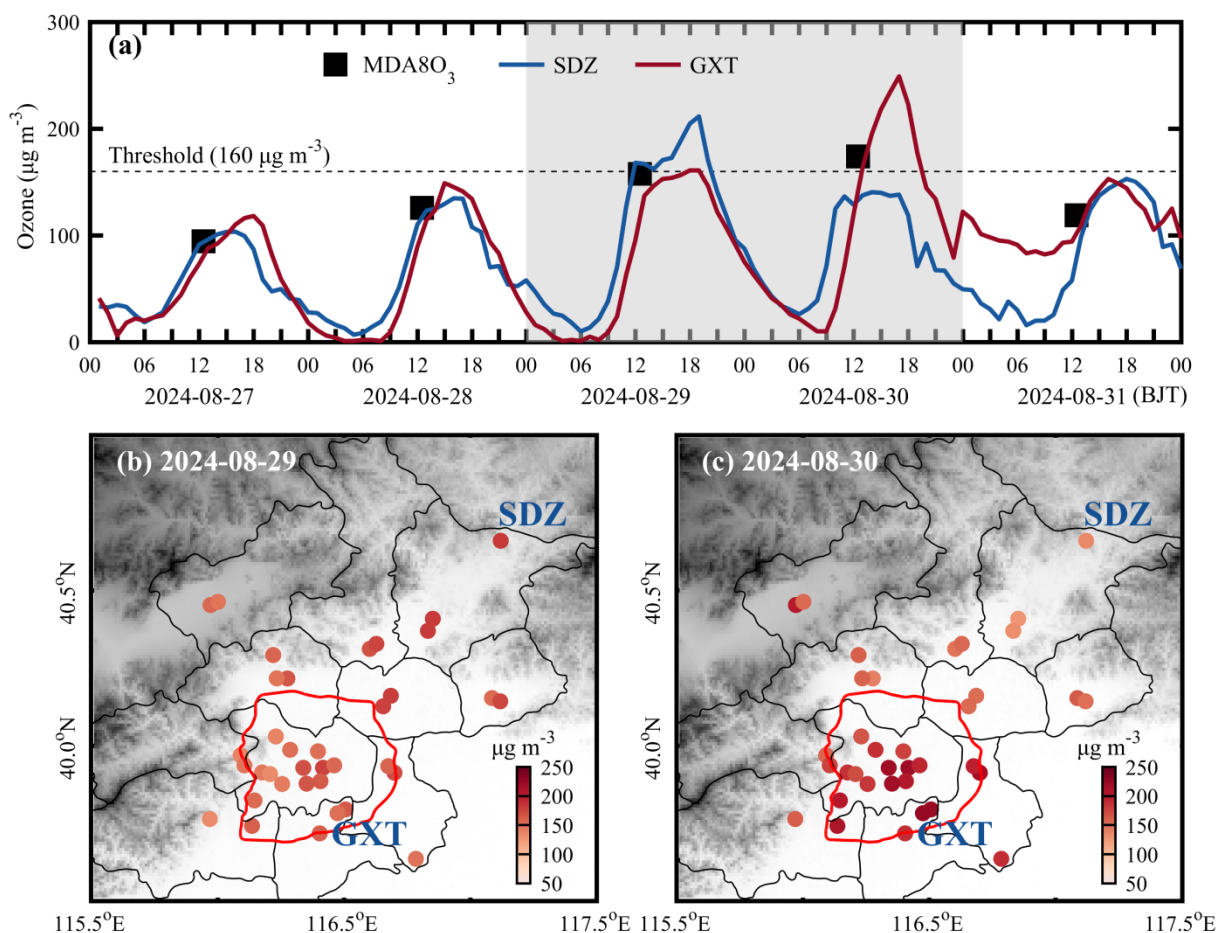
179 3. Results

180 3.1. Case study

181 3.1.1. Overview of the O₃ pollution episode

182 Following heavy rainfall on 26 August 2024, Beijing experienced consecutive sunny days until light rain
183 resumed on 31 August. The persistent sunny weather established favorable meteorological background for
184 photochemical O₃ production. Consequently, surface O₃ concentrations in Beijing exhibited a daily increasing trend
185 from 27 to 30 August. On the final two days (29 and 30 August), the city-averaged daily maximum 8-hour average
186 O₃ (MDA8O₃) concentrations approached or exceeded China's ambient air quality standard threshold of 160 μg m⁻³,
187 peaking at 174 μg m⁻³ on 30 August (Fig. 3a). A notable feature of these two polluted days was the stark contrast in
188 the spatial distribution of O₃ concentrations. On 29 August, the spatial pattern showed a positive O₃ gradient
189

190 extending northeastward, which was reversed on 30 August (Fig. 3b, c). This contrast was exemplified by the
 191 station observations: SDZ recorded its peak O₃ concentration (212 μg m⁻³ at 18:00 BJT) on 29 August, significantly
 192 higher than the concurrent value at GXT (161 μg m⁻³). Conversely, GXT observed its maximum O₃ level (249 μg
 193 m⁻³ at 16:00 BJT) on 30 August, far exceeding the measurement at SDZ (138 μg m⁻³; Fig. 3a). These contrasting
 194 spatial patterns seem to represent two typical O₃ pollution scenarios in Beijing: an urban plume transport pattern
 195 and an urban pollution accumulation pattern, as previously reported by Zong et al. (2023). The key question is what
 196 mechanism drove the rapid intensification of O₃ pollution and the reversal of its spatial pattern over the two
 197 consecutive days.

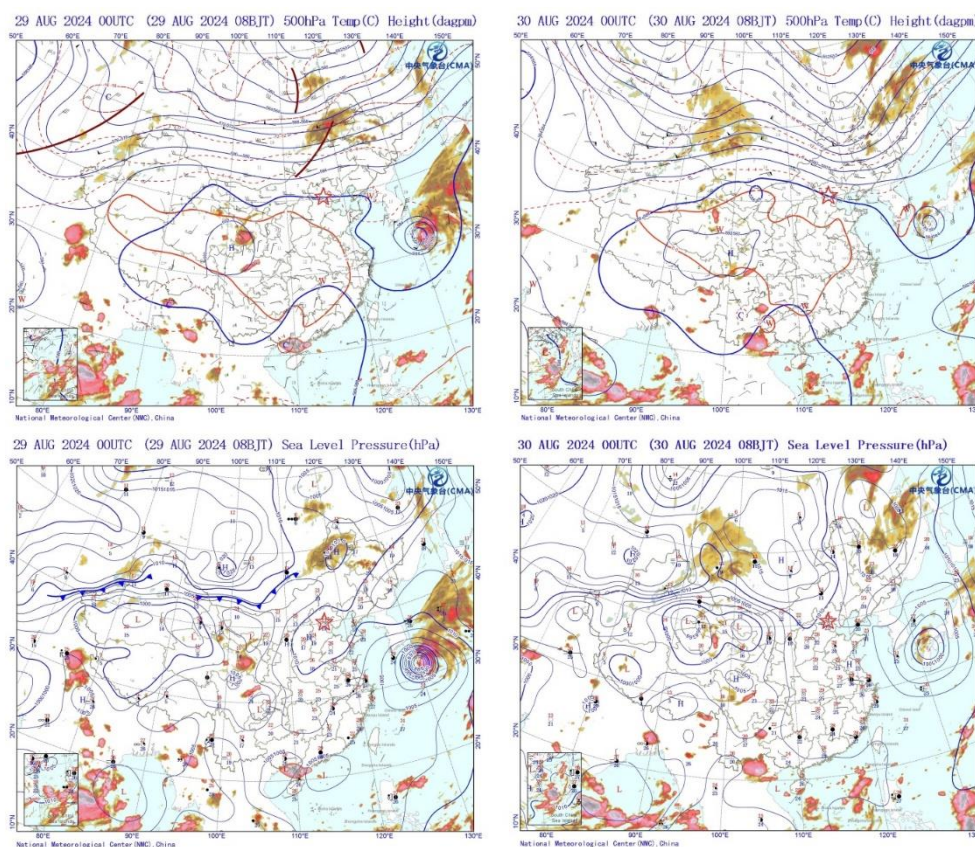


198
 199 **Figure 3.** (a) Time series of surface ozone concentrations at the GXT and SDZ stations from 27 to 31 August 2024;
 200 Spatial distribution of maximum 8-h O₃ concentrations over Beijing on (b) 29 and (c) 30 August. In (a), black
 201 squares represent the city-averaged MDA8O₃ concentrations; gray shading denotes the two polluted days (29 and
 202 30 August 2024).

203
 204 **3.1.2. Meteorological attribution to elevated foehn**

205 The weather charts at 08:00 BJT on 29 and 30 August are presented in Fig. 4. A subtropical high prevailed in the
 206 upper atmosphere over the central and eastern China, while a typhoon was active over the western Pacific Ocean
 207 south of Japan. The coexistence of these two synoptic systems induced widespread clear skies over the eastern
 208 China, a condition highly conducive to photochemical O₃ production (Ouyang et al., 2022; Shu et al., 2016). In the
 209 lower atmosphere, the synoptic patterns differed between the two days. On 29 August, the North China Plain (NCP)
 210 was under the influence of a weak high-pressure system. By 30 August, another high-pressure system (a cold front)

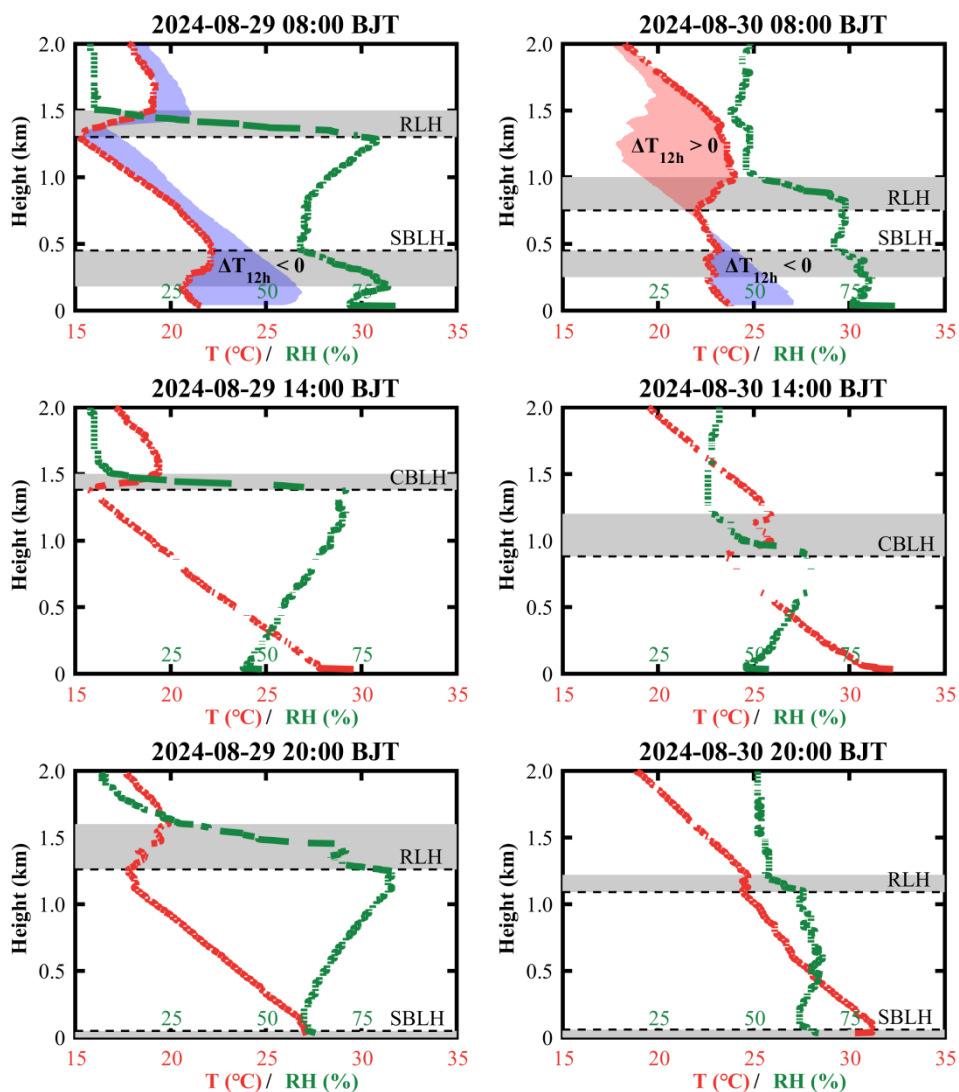
211 had intruded into the northwestern NCP from the Mongolian Plateau, creating a strong pressure gradient
212 perpendicular to the Taihang Mountains. Traditionally, cold fronts are known to have a significant clearance effect
213 on air pollutants (Zhang et al., 2021). However, in this case, the cold front led to an unexpected O₃ increase in
214 Beijing on 30 August. So, what underlying mechanism was responsible for this phenomenon?



215
216 **Figure 4.** Weather charts at 500 hPa and sea-level pressure over the East Asia at 08:00 BJT on 29 and 30 August,
217 2024. Shaded areas denote the cloud cover. The location of Beijing is marked by a red star.

218
219 To address the question above, we examined the radiosonde profiles and derived boundary layer heights at the
220 GXT station (Fig. 5). The results indicate that the CBLH and RLH on 30 August (750, 880, and 1090 m at 08:00,
221 14:00, and 20:00 BJT, respectively) were significantly lower than those on 29 August (1300, 1380, and 1260 m at
222 the same times), despite the SBLH showing no significant difference. The CBLH defines the available volume that
223 the pollutants emitted/produced near the surface can occupy, directly affecting their surface concentration and air
224 quality (Tang et al., 2016). Evidently, the significant decline in CBLH contributes to the surface O₃ enhancements
225 in urban Beijing on 30 August. Notably, the two-day CBLH difference originated from a sharp drop (more than 500
226 m) in RLH between 20:00 BJT on 29 August and 08:00 BJT on 30 August. Comparing radiosonde profiles from
227 these two time points revealed abnormal drying and warming in the residual layer, with a maximum temperature
228 increase of up to 5.8°C at 1250 m, contrasting sharply with the normal cooling observed the previous night. The
229 base height of this warming layer coincided precisely with the RLH observed at 08:00 BJT on 30 August,
230 indicating that the warming process was responsible for the overnight RLH drop and thereby contributed to the
231 subsequent daytime O₃ pollution exacerbation. Furthermore, the nocturnal residual layer warming inevitably
232 contributes to higher daytime air temperatures. As observed, the afternoon boundary layer temperature on 30
233 August showed a significant increase compared to the previous afternoon, and this higher temperature further
234 promotes photochemical O₃ production by accelerating photochemical reaction rates and enhancing emissions of

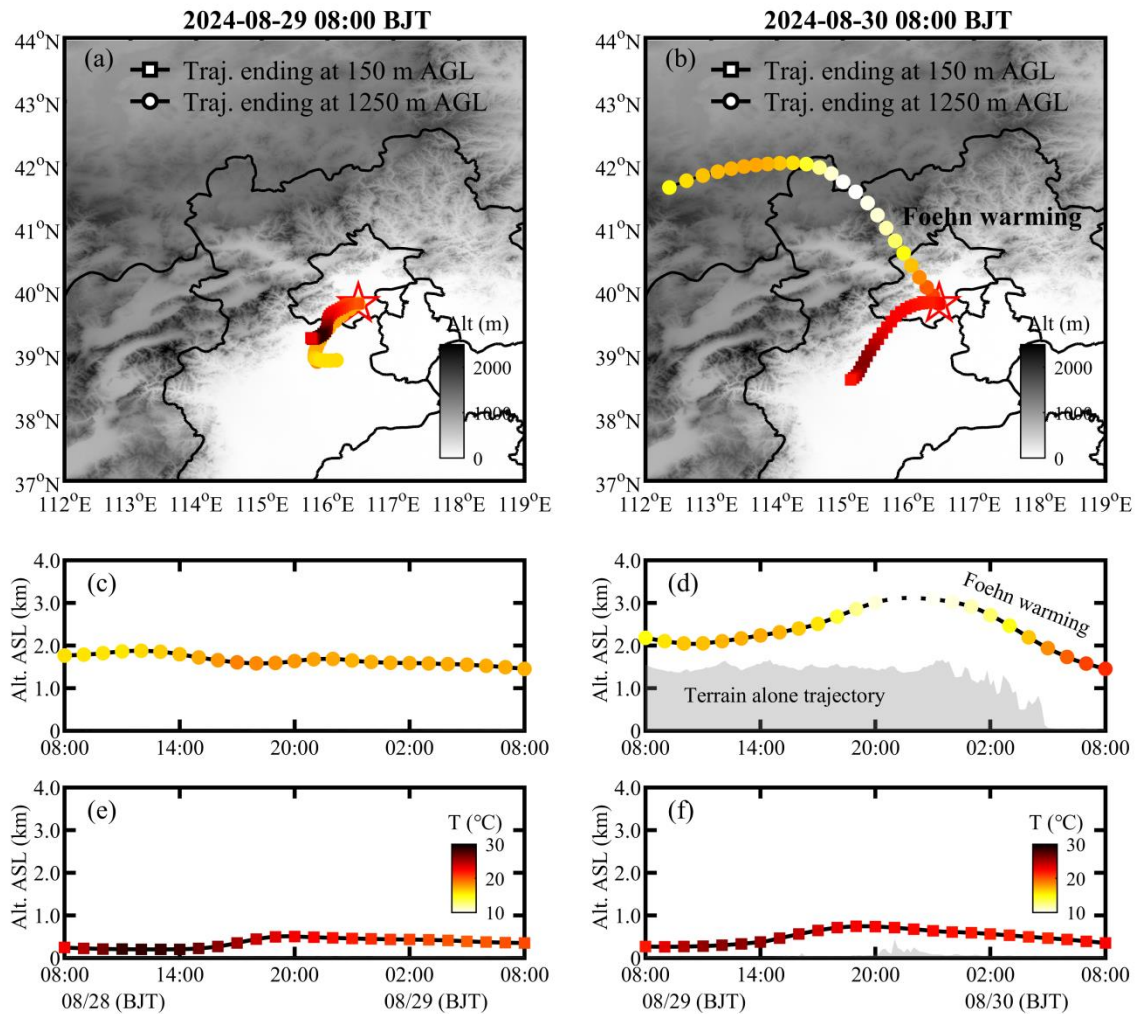
235 volatile organic compounds and soil nitric oxide (Gu et al., 2020; Wu et al., 2024). Thus, in addition to promoting
 236 daytime O₃ accumulation by reducing the boundary layer height, residual layer warming also enhances daytime
 237 photochemical O₃ production. Moreover, these changes in boundary layer thermal properties can facilitate O₃
 238 accumulation by lowering O₃ loss. For instance, the lowered CBLH can reduce the transport of PAN (peroxyacetyl
 239 nitrate, a NO_x reservoir in the upper atmosphere) into urban Beijing (a NO_x-saturated zone), which may suppress O₃
 240 loss from NO titration and independently contribute to the observed O₃ increases (Flowerday and Hansen, 2026).
 241 The remaining question is: what caused the abnormal warming of the nocturnal residual layer under the background
 242 of a cold front intrusion?



243
 244 **Figure 5.** Radiosonde-based temperature (T, red lines) and relative humidity (RH, green lines) profiles at the GXT
 245 station. Gray shaded areas represent the heights of temperature inversion layers. Dashed lines denote the afternoon
 246 convective boundary layer height (CBLH), and dot lines denote the nocturnal stable boundary layer height (SBLH).
 247 Colorful shaded areas highlight the overnight temperature changes, with increase marked in red and decrease in
 248 blue. Note: at 08:00 BJT (morning transition), emerging solar radiation collapses the near-surface SBL; thus, the
 249 SBLH at this time is determined at the top of the residual underlying temperature inversion.

250
 251 Using the HYSPLIT model, we traced the 24-hour origin and characteristics of the air mass at the overnight
 252 maximum warming height (1250 m) observed at 08:00 BJT on 30 August (Fig. 6b and d). For comparison, we also

253 calculated backward trajectories for the near-surface (150 m) airflow at the same time (Fig. 6b and f), as well as
 254 airflows at the same heights and time on the previous day (Fig. 6a, c, and e). The results show that the airflows at
 255 1250 m and 150 m on 29 August, as well as at 150 m on 30 August, all originated from the southern NCP region
 256 with no significant change in trajectory height. In contrast, the air mass at the maximum warming height on 30
 257 August originated from the Mongolian Plateau. It moved eastward to the northern side of the Yanshan Mountains,
 258 turned southeastward to cross the mountains, and finally arrived in Beijing. During this transport, the airflow first
 259 ascended about 1000 m and then descended about 1500 m, accompanied by a temperature change of cooling (7.6°C)
 260 followed by warming (11.4°C). These changes in trajectory height and temperature exhibit very pronounced foehn
 261 warming characteristics (Elvidge and Renfrew, 2016). Previous studies have reported several cases of shallow
 262 foehn-induced nocturnal surface warming in Beijing (Li et al., 2026; Luo et al., 2020). Our case differs significantly
 263 because it involves elevated air masses and shows no warming in the surface layer. To confirm this, we examined
 264 hourly temperature variations from 20:00 BJT on 29 August to 08:00 BJT on 30 August at 20 surface
 265 meteorological stations in Beijing (Fig. S3), as well as at 15 levels on a 325 m high meteorological tower (Fig. S4).
 266 The results revealed that, except for the high-altitude Foyeding station (1224.9 m), no temperature surges
 267 ($\Delta T_{1h} > 1^\circ\text{C}$) were observed before sunrise (around 06:00 BJT) at the other stations. This implies no detectable
 268 foehn warming signature from standard mountain-leeside surface observations (Li et al., 2025), despite the strong
 269 foehn signature in the residual layer. Therefore, we identify this case as the first observation of a novel type of
 270 foehn phenomenon in Beijing: elevated foehn in the residual layer.

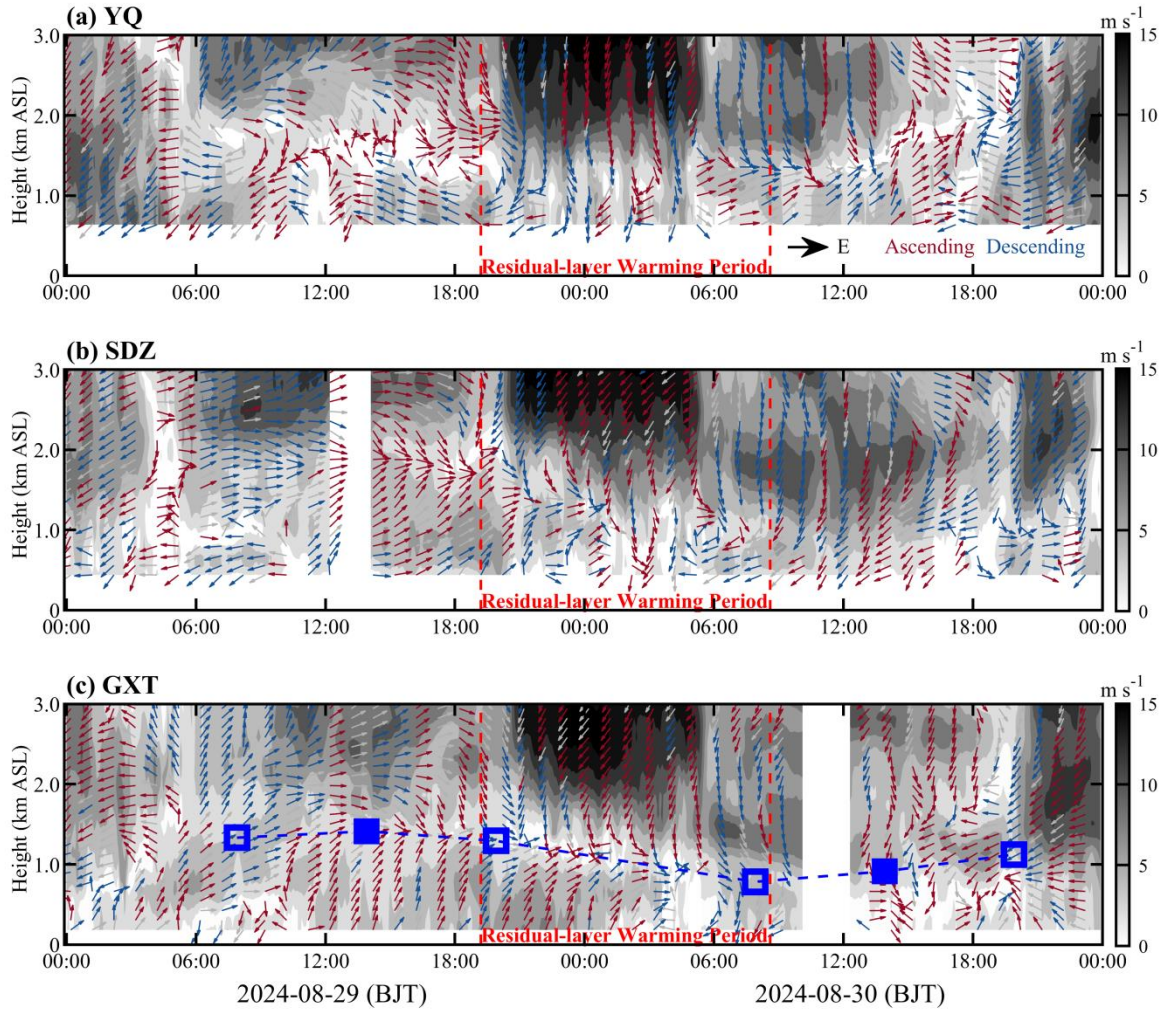


271 **Figure 6.** 24-h backward trajectories ending at 150 m (squares) and 1250 m (dots) above ground level (AGL) over
 272

273 the GXT station, at 08:00 BJT of (a) 29 and (b) 30 August. The 1250 m level corresponds to the maximum
274 overnight warming height at 08:00 BJT on 30 August (see Fig. 5). Panels (c-f) show the height and temperature
275 changes of 24-h backward trajectories at 150 and 1250 m. All temperature changes share the same colorbar,
276 including those in (a) and (b).

277

278 To illustrate the dynamical conditions during the elevated foehn-induced residual layer warming, Figure 7 presents
279 the radar wind profiles at the YQ, SDZ, and GXT stations from 29 to 30 August. Prior to the warming, southerly
280 winds prevailed in the boundary layer (southwesterly at SDZ and GXT; southeasterly at YQ), while lower
281 free-tropospheric winds gradually shifted from southwesterly to northwesterly. After sunset on 29 August, the cold
282 front intrusion induced strong northeasterly winds in the lower free troposphere at all stations. These northeasterly
283 winds aloft first descended into the boundary layer at YQ, followed by SDZ. In contrast, GXT maintained
284 southwesterly boundary-layer winds until later in the night, forming a distinct northwesterly wind shear zone aloft.
285 During this process, the height of the northwesterly wind shear corresponded well with the sounding-derived RLH
286 at GXT, and the northwesterly winds matched the HYSPLIT backward trajectories ending at GXT (Fig. 6b).
287 Combining the HYSPLIT results, these features strongly support the mechanism of an elevated northwesterly foehn
288 during the residual layer warming period. The elevated foehn appears to have occurred within a shallow wind shear
289 zone, similar to the elevated foehn scenario reported in winter Urumqi by Li et al. (2015). After the residual layer
290 warming, northeasterlies prevailed in the boundary layer at SDZ and southwesterlies at YQ, whereas GXT showed
291 highly variable winds with weak speeds—likely due to convergence between the emerging northwesterly foehn and
292 the prevailing southwesterly flows. This weak-wind stagnant condition suppressed the horizontal dispersion of air
293 pollutants. Operating in conjunction with the inhibited vertical dispersion (from a lower boundary layer height) and
294 accelerated photochemical production (due to higher temperatures), this post-foehn convergent stagnation represents
295 a third contributing factor to the severe daytime O₃ pollution observed in urban Beijing on 30 August.



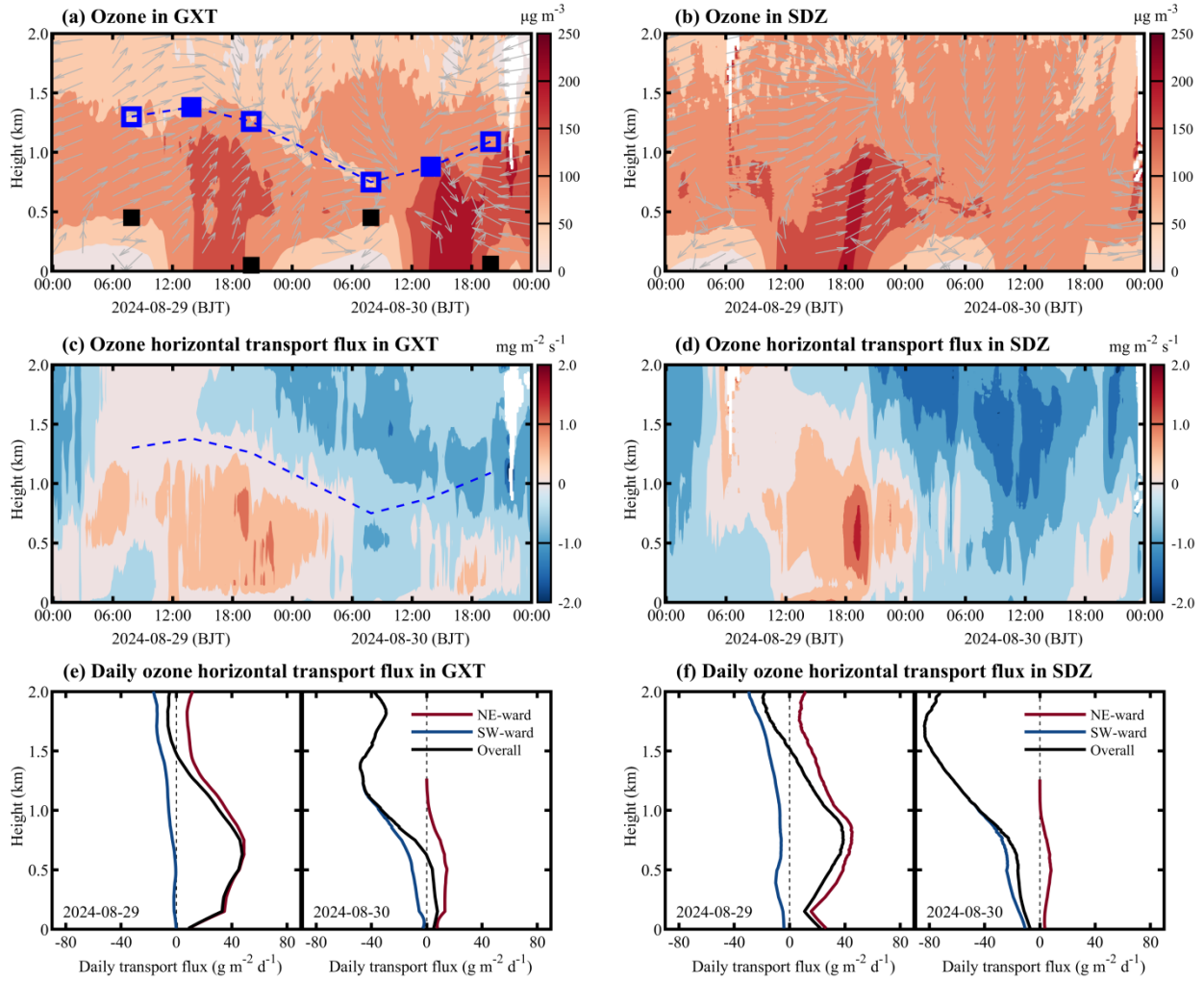
296

297 **Figure 7.** Radar-based wind profiles at the (a) YQ, (b) SDZ, and (c) GXT stations before, during, and after the
 298 elevated foehn-induced residual layer warming. Shaded areas represent horizontal wind speed; arrows denote
 299 horizontal wind direction (red indicates ascending motion, blue indicated descending motion). In (c), blue squares
 300 denote the convective boundary layer height (solid) or residual layer height (hollow); blue dashed line indicates the
 301 evolution of the convective boundary layer and residual layer heights.

302

303 3.1.3. Three-dimensional evolution of O₃ before, during, and after elevated foehn

304 The coordinated O₃ lidar observations at the urban (GXT) and rural (SDZ) stations provided a unique
 305 opportunity to elucidate the three-dimensional evolution of boundary-layer O₃ in response to elevated foehn. By
 306 integrating data from meteorological radiosondes and radar wind profilers, we investigated how sudden changes in
 307 boundary layer thermal and dynamical structure induced by elevated foehn affected O₃ evolution and quantified the
 308 differences in boundary layer O₃ transport fluxes between the pre- and post-foehn days (Fig. 8).



309

310 **Figure 8.** Vertical O₃ concentrations, wind direction, and O₃ transport flux at the GXT and SDZ stations. In (a),
 311 squares denote the boundary layer heights determined from radiosonde profiles (black for SBLH, blue for
 312 CBLH/RLH). The blue dashed line in (a) and (c) indicates the evolution of CBL and RL heights. In (c) and (d),
 313 positive (negative) horizontal transport flux indicates northeastward (southwestward) transport in the direction from
 314 GXT to SDZ. Panels (e) and (f) show the daily integrated O₃ transport flux at the GXT and SDZ stations on 29 and
 315 30 August, respectively.

316

317 As shown in Fig. 8a, the boundary layer thermal structure critically shaped O₃ vertical distribution in urban
 318 Beijing: a steep gradient in the SBL, an O₃ reservoir in the RL, and relatively uniform mixing in the CBL. The
 319 elevated foehn-induced residual layer warming on the night of 29–30 August led to a significant reduction in the
 320 boundary layer height on 30 August, substantially compressing the vertical space for daytime O₃ mixing. Combined
 321 with enhanced photochemical O₃ production (due to higher temperatures) and weakened horizontal dispersion (due
 322 to lower post-foehn wind speeds,) these factors collectively contributed to a marked increase in afternoon boundary
 323 layer O₃ concentrations in urban Beijing on 30 August (200–250 $\mu\text{g m}^{-3}$) compared to the previous day ($\sim 150 \mu\text{g m}^{-3}$).
 324 We also observed that the elevated foehn was accompanied by downward transport of free-tropospheric O₃
 325 (Fig. 8a). However, due to the presence of a strong capping inversion acting as a transport barrier (Fig. 5), this
 326 descending free-tropospheric O₃ was unlikely to have significantly intruded into the boundary layer.

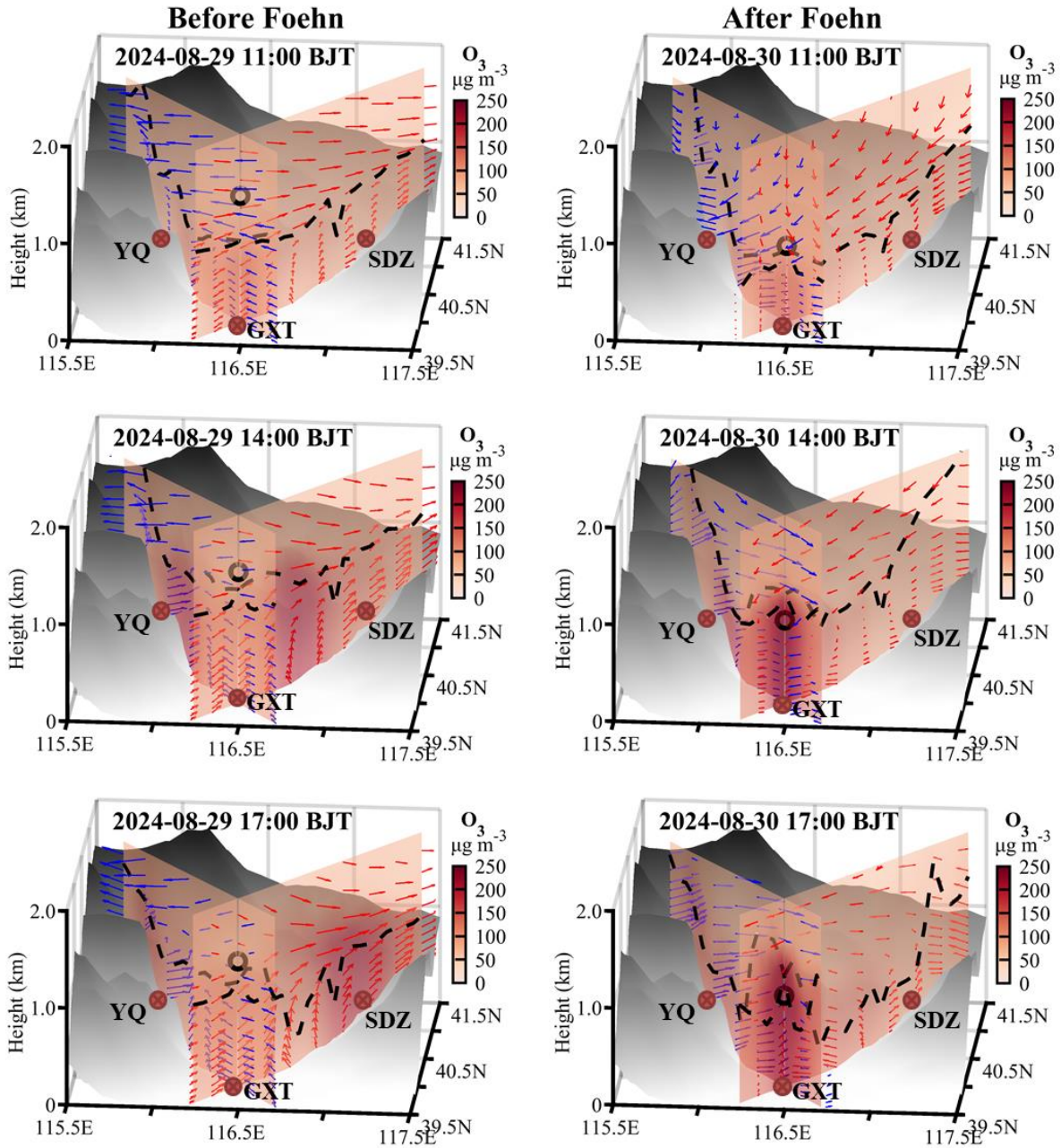
327

328 The urban-rural coordinated lidar observations clearly reveal a dynamically driven shift in spatial heterogeneity

329 before and after the elevated foehn. On 29 August (pre-foehn), prevailing southwesterly flows facilitated the
330 northeastward transport of the urban O₃ plume. The lidars recorded higher O₃ concentrations at the downwind rural
331 SDZ station than at the urban GXT station (Fig. 8a and b). The peak O₃ occurrence at SDZ was delayed by 1–3
332 hours relative to GXT, consistent with advective transport. The calculated horizontal O₃ transport flux was
333 predominantly northeastward in the boundary layer at both stations throughout the day, with stronger fluxes in the
334 upper boundary layer. The instantaneous maximum flux at SDZ exceeded 2.0 mg m⁻³ s⁻¹, significantly higher than
335 at GXT (Fig. 8c and d). In stark contrast, the post-foehn convergence stagnation on 30 August suppressed advective
336 transport and promoted local O₃ accumulation in urban Beijing. Consequently, afternoon boundary layer O₃
337 concentrations at GXT reached notably high levels (200–250 µg m⁻³), while concentrations at SDZ dropped to low
338 values (~100 µg m⁻³). Despite this spatial contrast, the boundary layer O₃ transport flux at both stations was
339 markedly low compared to the previous day (Fig. 8c, d, e, and f), underscoring a shift in the dominant pollution
340 mechanism from urban plume transport to urban pollution accumulation.

341

342 We examined the WRF-Chem output to gain further insight into the vertical O₃ structure over Beijing before and
343 after the elevated foehn. As shown in Fig. 9, although the WRF-Chem model exhibited some deviations in
344 simulating the boundary layer height, it successfully reproduced the pre-foehn northeastward transport of the urban
345 O₃ plume on 29 August, as well as the post-foehn stagnation-driven local O₃ accumulation in the urban Beijing on
346 30 August. On 29 August, the O₃ pollution initially built up in the urban area (e.g., near GXT) by 11:00 BJT. By
347 14:00 BJT, the high-O₃ zone had shifted to the northern suburbs, and by 17:00 BJT, it had been transported to the
348 rural areas in the northeast (e.g., near SDZ). In contrast, on 30 August, the relatively higher O₃ concentrations over
349 Beijing were consistently confined in the urban area, with no significant spatial shift. These simulation results
350 aligned well with the lidar observations. Furthermore, the WRF-Chem model reproduced the vertical wind patterns
351 observed at GXT, SDZ, and YQ (Fig. 7), thereby better illustrating the vertical structure of the foehn flow during its
352 decaying stage on 30 August via wind cross-sections. The foehn simulations show that while the near-surface
353 component—shallow foehn—was blocked by prevailing southerly winds within the boundary layer, leading to
354 convergence and airflow stagnation over urban Beijing, its upper-layer branch—elevated foehn—passed directly
355 over the urban area unimpeded, resulting in persistent warming that suppressed the daytime convective boundary
356 layer development until the foehn decayed around 14:00 BJT. These features are evident in both the GXT-YQ
357 cross-section (parallel to the elevated northwesterly foehn) and the GXT-SDZ cross-section (perpendicular to the
358 elevated northwesterly foehn). The configuration of an unimpeded elevated foehn and a blocked shallow foehn
359 effectively explains the accumulation of higher O₃ concentrations in the urban boundary layer of Beijing on 30
360 August.



361

362 **Figure 9.** Cross-sections of simulated O_3 concentrations along the line across the GXT and SDZ stations and the
 363 line across GXT and YQ stations on 29 and 30 August. Dashed black lines denote the simulated boundary layer
 364 height, and arrows show the composite of simulated horizontal wind speed ($m s^{-1}$) and vertical wind speed ($\times 10 m$
 365 s^{-1}) in the GXT-SDZ (red arrows) and GXT-YQ (blue arrows) cross-sections. Only horizontal wind speed in the
 366 direction along the individual cross-sections is included. The black dots denote the boundary layer height observed
 367 at GXT and the height at 14:00 BJT is the observational value and these at 11:00 and 17:00 BJT are interpolated
 368 from two adjacent radiosonde observations.

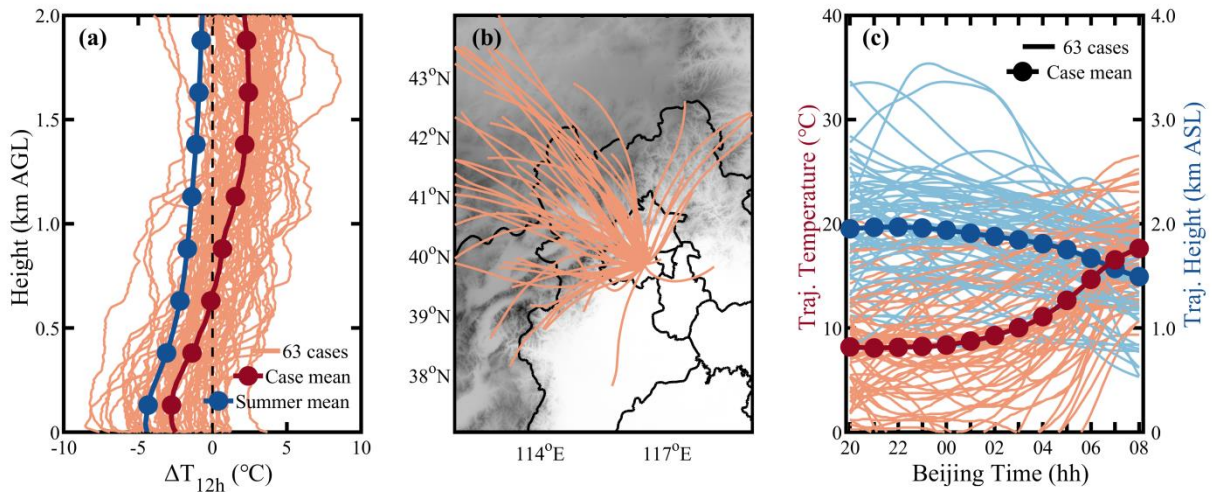
369

370 3.2. Climatological evaluation

371 While a case study is valuable for mechanistic understanding, the question of representativeness always arises.
 372 To clarify whether the features identified in the case study are typical, we supplemented the case analysis with a
 373 climatological investigation of elevated foehn and its O_3 pollution effect based on long-term observations.

374

375 Based on summer radiosonde data from the GXT station during 2015-2024, we calculated overnight temperature
 376 change (ΔT_{12h}) profiles for each night by differencing the temperature profiles at 20:00 BJT and 08:00 BJT the
 377 following day. We identified a residual layer warming event when $\Delta T_{12h} > 3^\circ\text{C}$ occurred within 500-2000 m height
 378 range. For each event, we identified the height of maximum warming and used it as the endpoint for backward
 379 trajectory calculations. Statistical results show that among the 920 valid summer observation days from 2015 to
 380 2024, a total of 63 residual layer warming cases were identified, accounting for 6.85% of summer night. Figure 10
 381 illustrates the ΔT_{12h} profiles, backward trajectories, and trajectory height/temperature changes for these events.
 382 While warming heights vary widely across different events, the composite ΔT_{12h} profile highlights warming above
 383 ~650 m, contrasting sharply with the summer mean profile showing nocturnal cooling throughout the layer. The
 384 backward trajectories of these warming air masses show that most originated from high-altitude regions to the west
 385 or north. After crossing the Yanshan or Taihang Mountains, these airflows arrived in Beijing, with their trajectories
 386 descending on average by 500 m and their temperature rising rapidly by an average of 10°C , exhibiting clear foehn
 387 characteristics. Applying the elevated foehn criteria from Sect. 2.2, 54 of the 63 warming cases (85.7%) can be
 388 attributed to elevated foehn. These results confirm that elevated foehn is the primary cause of nocturnal residual
 389 layer warming in Beijing.



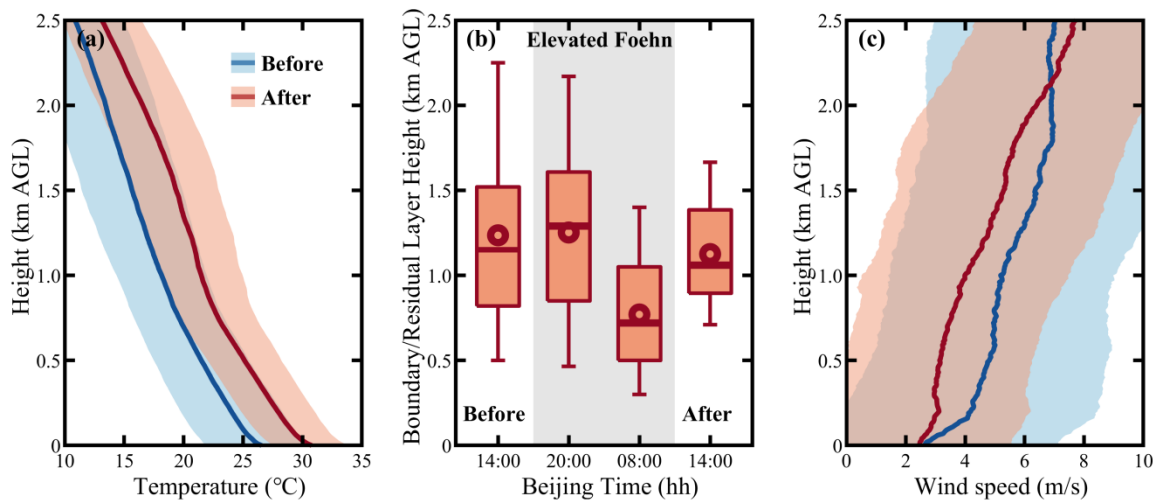
390

391 **Figure 10.** (a) Overnight temperature change (ΔT_{12h}) profiles from 20:00 BJT to next-day 08:00 BJT, (b) overnight
 392 airflow backward trajectories ending at the maximum warming height, and (c) overnight trajectory height and
 393 temperature changes for the 63 identified residual layer warming events.

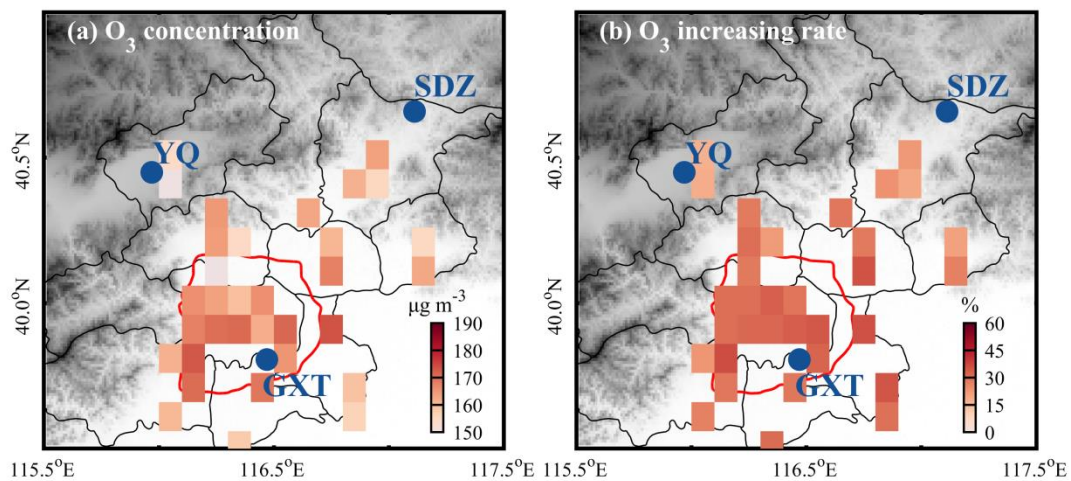
394

395 Previous case analysis indicated that elevated foehn exacerbates next-day O_3 pollution through three pathways:
 396 increasing boundary layer temperature (enhancing photochemistry), reducing boundary layer height (inhibiting
 397 vertical diffusion), and weakening boundary layer winds (suppressing horizontal dispersion). Composite analyses
 398 of all 54 elevated foehn events (Fig. 11) strongly support the prevalence of these mechanisms. On average,
 399 post-foehn afternoon boundary layer temperature was more than 3°C higher than pre-foehn conditions. The
 400 elevated foehn-induced residual layer warming directly led to an average RLH reduction of 480 m, and the
 401 subsequent afternoon CBLH was, on average, 110 m lower. Post-foehn afternoon boundary layer wind speed
 402 decreased by more than 1.0 m s^{-1} on average. Overall, these meteorological changes consistently favor local O_3
 403 production and accumulation. As a result, approximately 87 % of elevated foehn events were followed by worsened
 404 O_3 pollution. Post-foehn MDA8O_3 concentrations across Beijing increased by an average of 20–60% (varying by
 405 site) compared to the preceding day (Fig. 12b). Within the main urban zone (inside the 6th Ring Road), the

406 MDA8O₃ increase generally exceeded 45% (Fig. 12b), with concentrations commonly surpassing the national air
 407 quality standard of 160 μg m⁻³ (Fig. 12a).



408
 409 **Figure 11.** Composite of (a) afternoon boundary layer temperature profiles, (b) boundary/residual layer height, and
 410 (c) afternoon boundary layer wind speed profiles before, during, and after 54 identified elevated foehn events in
 411 Beijing. In (a) and (c), solid lines denote the mean profiles and shaded areas represent the standard deviation. In (b),
 412 box-and-whisker plots show the 5th, 25th, 50th, 75th, and 95th percentiles; dots represent the means.



413
 414 **Figure 12.** Composite of (a) daily maximum 8-h O₃ concentrations following elevated foehn in Beijing, and (b)
 415 their average percentage increase compared to preceding days. Note: site data are resampled and shown on a
 416 0.1°×0.1° grid, accounting for the relocation of some sites around 2021.

417
 418 **4. Discussion**

419 Traditionally, nocturnal warming has been considered rare. Previous studies have observed occasional nighttime
 420 surface warming in leeward plains or valleys due to foehn effects (Luo et al., 2020; Ma et al., 2015). This study, by
 421 creatively integrating radiosonde data, reveals for the first time the frequent occurrence of pronounced nocturnal
 422 residual layer warming in summer Beijing. The primary driver is identified as elevated foehn—an upper-layer
 423 phenomenon previously missed by near-surface observations. Theoretically, unlike near-surface warming from
 424 shallow foehn (which enhances boundary layer instability), residual layer warming from elevated foehn reinforces
 425 static stability (Stull, 1988). Our observations show that the elevated foehn-induced warming substantially lowers

426 the boundary layer capping inversion (i.e., RLH), thereby inhibiting the development of the next day's convective
427 boundary layer. While Pal and Lee (2019) highlighted that mountain air mass advection can lead to boundary layer
428 overrunning over downwind plains, our results demonstrate that under elevated foehn, mountain-sourced air masses
429 can instead act to lower the downwind boundary layer height through foehn warming.

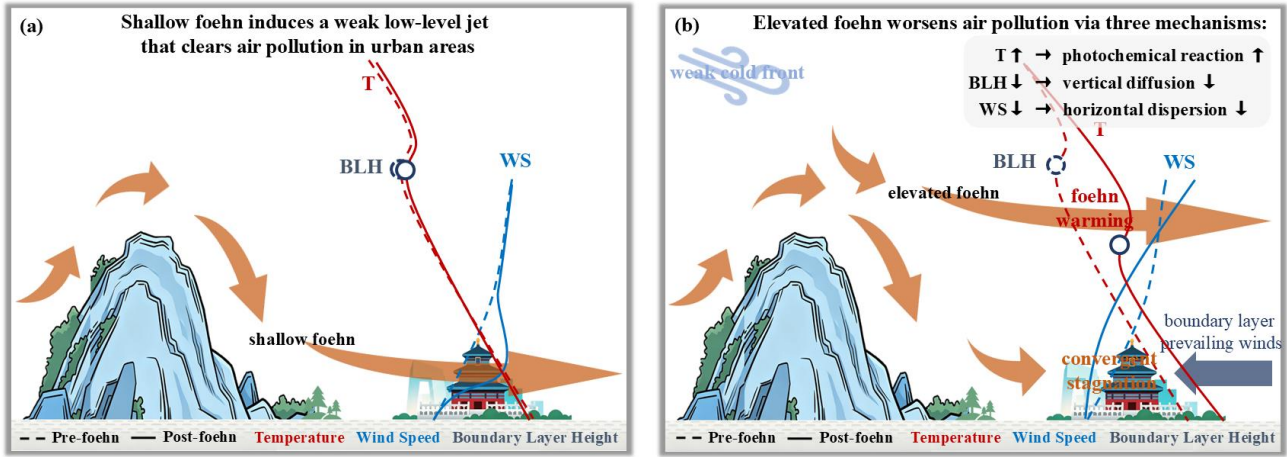
430

431 The elevated foehn process in summer Beijing shows both similarities and differences with that in winter Urumqi
432 (Li et al., 2015). The similarity lies mainly in the three-layer flow structure that causes similar "sandwich" foehn
433 warming within a middle wind shear layer. The key difference lies in the post-foehn boundary layer convergence
434 mechanism. In winter Urumqi, a downslope wind and hydraulic jump occur simultaneously on the northern leeside
435 of the Tianshan Mountains after the foehn encounters a cold air pool in the southern suburbs, generating
436 convergence between the cold pool and the shallow downslope wind (Li et al., 2015). In contrast, no such cold air
437 pool exists in summer Beijing. Here, the post-foehn convergence instead results from the confrontation between the
438 emerging northwestern foehn winds and the prevailing southwestern winds within the boundary layer. The
439 relatively strong boundary-layer southwesterly winds appear to be a necessary prerequisite for the occurrence of
440 elevated foehn in summer Beijing, as they inhibit the intrusion of shallow foehn toward plain areas and, in turn,
441 force the foehn to develop upward. In other words, the relatively strong boundary-layer southwesterly winds in
442 summer Beijing likely play a role similar to that of the cold air pool in winter Urumqi in lifting the foehn to form an
443 elevated foehn.

444

445

446 Our results reveal that 86.9% of the identified elevated foehn events were followed by O₃ pollution exacerbation
447 in summer Beijing. Post-foehn MDA8O₃ concentrations increased more than 30% on average, exceeding the
448 national pollution threshold at most monitoring sites. In a previous study, Li et al. (2025) explored connections
449 between ground-based (shallow) foehn and PM_{2.5} pollution in Beijing, finding that 60.4 % of cases corresponded to
450 pollution mitigation and only 39.6% to exacerbation. Given that direct comparability is limited due to differences in
451 pollutant (PM_{2.5} vs. O₃), season (annual vs. summer), and foehn type (shallow vs. elevated), we acquired the
452 summertime shallow foehn dates identified in Li et al. (2025) and conducted additional statistics of air pollution for
453 summertime shallow foehn events (Table S1). The statistics indicated that elevated foehn corresponds to a
454 markedly higher probability (86.9%) of post-foehn O₃ pollution exacerbation compared to shallow foehn (55.2%).
455 Similar results are found for PM_{2.5} pollution (69.8% vs. 55.2%). These results clearly indicate that elevated foehn
456 exhibits a more deterministic pollution-worsened effect than shallow foehn. Furthermore, we examined the changes
457 in boundary layer structure before and after summertime shallow foehn events (Fig. S5). The results revealed no
458 significant changes in boundary layer temperature or boundary layer height. However, shallow foehn tends to
459 induce a weak low-level jet, which can clear air pollution in urban areas and thereby inhibit pollution exacerbation.
460 In light of the above comparison, we summarized a conceptual diagram in Fig. 13 to illustrate the distinct pollution
461 mechanisms associated with shallow versus elevated foehn. Overall, elevated foehn can serve as a more reliable
462 meteorological precursor for O₃ pollution warnings in summer Beijing. Since elevated foehn can be directly
463 identified from routine radiosonde observations (Sect. 2.2), its application as a precursor for summer O₃ forecasting
464 can be both highly convenient and timely.



465

466 **Figure 13.** Conceptual diagram illustrating the distinct pollution mechanisms associated with shallow versus
 467 elevated foehn.
 468

469

5. Conclusion

470

This study systematically investigated the formation process of elevated foehn winds and their mechanisms for exacerbating surface O₃ pollution in summer Beijing through a combined case analysis and climatological evaluation. The main conclusions are as follows:

471

472

473

1、 First observational confirmation of elevated foehn events in summer Beijing. Utilizing high-resolution radiosonde observations, this study identified a novel phenomenon distinct from traditional near-surface foehn. It manifests as abnormal nocturnal warming ($\Delta T_{12h} > 3^{\circ}\text{C}$) within the elevated residual layer (approximately 500–2000 m AGL), with no significant warming signal at the surface. Lagrangian back-trajectory analysis confirms that the warming air masses originate from the northwestern or northern plateaus, undergoing descent and warming after crossing the Yanshan or Taihang Mountains, exhibiting classic foehn characteristics. These elevated foehn events account for 5.87% of summer nights and are identified as the primary driver (85.7% of identified cases) of nocturnal residual layer warming in Beijing.

474

475

476

477

478

479

480

481

2、 Clarification of the triple synergistic mechanisms through which elevated foehn exacerbates next-day O₃ pollution. Thermodynamic Effect I: Increasing boundary layer temperature to enhance photochemical production. Nocturnal residual layer warming directly leads to a significantly higher daytime boundary layer temperature (average increase $> 3^{\circ}\text{C}$), accelerating the photochemical reaction rates of precursors. Thermodynamic Effect II: Lowering the boundary layer height to suppress vertical diffusion. The residual layer warming reinforces atmospheric stability, causing the capping inversion base (i.e., the residual layer height) to drop by an average of ~ 480 m and the subsequent afternoon convective boundary layer height to decrease by ~ 110 m. This substantially compresses the vertical mixing volume for pollutants. Dynamic Effect: Inducing boundary-layer convergent stagnation to weaken horizontal transport. The intruding northwesterly elevated foehn flow confronts the prevailing southwesterlies within the boundary layer, forming a convergence zone. This leads to a marked reduction in wind speed (average decrease $> 1.0 \text{ m s}^{-1}$), severely hindering the horizontal advective dispersion of pollutants.

482

483

484

485

486

487

488

489

490

491

492

3、 Decade-long climatological evaluation confirms the highly deterministic and prevalent exacerbating effect of elevated foehn on summer O₃ pollution. Composite analysis of 54 identified elevated foehn events from 2015–2024 robustly supports the proposed mechanisms. Statistics show that 87% of elevated foehn events were followed by worsened O₃ pollution the next day. The city-wide MDA_{8O₃} concentration increased by 20–60% on average compared to the preceding day, with increases in the main urban area typically exceeding 45%.

493

494

495

496

497

498 Post-foehn MDA8O₃ concentrations commonly surpassed the national ambient air quality standard (160 µg
499 m⁻³). This stands in sharp contrast to additional statistics based on near-surface observations, which associate
500 shallow foehn primarily with no significant pollution changes, highlighting the fundamental difference in
501 pollution potential between shallow and elevated foehn.
502

503 In summary, this study identifies elevated foehn as a significant and previously overlooked meteorological
504 forcing factor for summer O₃ pollution in Beijing. Its synergistic "warming-lowering-stagnating" effects lead to a
505 highly deterministic pollution exacerbation. Given that elevated foehn can be directly identified using routine
506 radiosonde data, we propose its utility as a reliable and efficient meteorological precursor for O₃ pollution
507 forecasting and warning in Beijing and other cities with similar topography. This provides a new scientific basis for
508 the precise prevention and control of air pollution. Future research should focus on quantifying the contribution of
509 elevated foehn to O₃ generation under different synoptic backgrounds and exploring its coupling with regional
510 transport and chemical processes.
511

512 To date, numerous circulation classification-based studies have highlighted the importance of synoptic-scale
513 weather on regional O₃ pollution in the NCP region (Dong et al., 2020; Han et al., 2020; Liao et al., 2024; Liu et al.,
514 2019). However, day-to-day circulation classifications actually overlook sub-daily meteorological processes, such
515 as the nocturnal elevated foehn identified in this study. A very recent study (Xu et al., 2026) indicated that
516 ground-based foehns on the eastern Taihang Mountains preferentially occur under stable atmospheric stratification,
517 with a surface high over the windward side and a low over the leeward side, together with an upper-level cold
518 trough at 500 hPa and pronounced subsidence at 850 hPa on the leeward side on the eastern foothills of the Taihang
519 Mountains. However, this study did not extend its findings to the field of air pollution, nor did it clarify whether the
520 aforementioned synoptic conditions are also conducive to the occurrence of elevated foehn. Overall, a better
521 coupling of synoptic-scale circulation patterns and local-scale elevated foehn processes will further deepen our
522 understanding of meteorological mechanisms underlying O₃ pollution.
523

524 ***Code and data availability.***

525 Hourly surface ozone data, except for those from the SDZ station, were obtained from the China National
526 Environmental Centre (<http://www.cnemc.cn/en/>). The HYSPLIT model and its compatible meteorological data
527 were sourced from the NOAA Air Resources Laboratory (<https://www.ready.noaa.gov/HYSPLIT.php>). We are not
528 authorized to publicly release the following raw data: hourly ozone measurements at the SDZ station, radiosonde
529 data, ozone lidar observations, wind profiler radar measurements, and numerical simulation outputs. These datasets
530 are available from the corresponding author upon reasonable request (zqma@ium.cn).
531

532 **Author contributions**

533 Z.L. conceived the original idea, analyzed the data, and wrote the first version manuscript. J.X. conducted the
534 WRF-Chem simulation. L.Z. operated the remote sensing equipment. C.L. performed the HYSPLIT model. Z.M.
535 supervised the research project. All authors discussed the results and commented on the manuscript.
536

537 **Competing interests**

538 The authors declare no competing interests.
539

540 **Acknowledgements**

541 This research has been supported by the National Natural Science Foundation of China (Grant Nos. 42405115 and

542 42307150), and the Scientific Research Project of the Beijing Meteorological Bureau (Grant No.
543 BMBKJ202404002). We acknowledge the DeepSeek for polishing our English language. We thank the two
544 anonymous reviewers for their comments, which have greatly improved the quality of the manuscript.

545

546 **References**

- 547 Baumann, K., Maurer, H., Rau, G., Piringer, M., Pechinger, U., Prévôt, A., Furger, M., Neining, B., Pellegrini, U., 2001.
548 The influence of south Foehn on the ozone distribution in the Alpine Rhine valley—results from the MAP field phase.
549 *Atmospheric Environment* 35, 6379-6390.
- 550 Campana, M., Li, Y., Staehelin, J., Prevot, A.S.H., Bonasoni, P., Loetscher, H., Peter, T., 2005. The influence of south foehn
551 on the ozone mixing ratios at the high alpine site Arosa. *Atmospheric Environment* 39, 2945-2955.
- 552 Dong, Y.M., Li, J., Guo, J.P., Jiang, Z.J., Chu, Y.Q., Chang, L., Yang, Y., Liao, H., 2020. The impact of synoptic patterns on
553 summertime ozone pollution in the North China Plain. *Sci Total Environ* 735.
- 554 Elvidge, A.D., Renfrew, I.A., 2016. The Causes of Foehn Warming in the Lee of Mountains. *Bulletin of the American
555 Meteorological Society* 97, 455-466.
- 556 Flowerday, C., Hansen, J.C., 2026. Peroxyacetyl Nitrate (PAN) in the Atmosphere: A Comprehensive Review of Chemistry,
557 Measurements, and Chemical-Transport Implications. *Environmental Science: Atmospheres*.
- 558 Gaffin, D.M., 2002. Unexpected Warming Induced by Foehn Winds in the Lee of the Smoky Mountains. *Weather and
559 Forecasting* 17, 907-915.
- 560 Gaffin, D.M., 2009. On High Winds and Foehn Warming Associated with Mountain-Wave Events in the Western Foothills
561 of the Southern Appalachian Mountains. *Weather and Forecasting* 24, 53-75.
- 562 Grell, G.A., Peckham, S.E., Schmitz, R., McKeen, S.A., Frost, G., Skamarock, W.C., Eder, B., 2005. Fully coupled “online”
563 chemistry within the WRF model. *Atmospheric Environment* 39, 6957-6975.
- 564 Gu, Y., Li, K., Xu, J., Liao, H., Zhou, G., 2020. Observed dependence of surface ozone on increasing temperature in
565 Shanghai, China. *Atmospheric Environment* 221, 117108.
- 566 Guenther, A., Karl, T., Harley, P., Wiedinmyer, C., Palmer, P.I., Geron, C., 2006. Estimates of global terrestrial isoprene
567 emissions using MEGAN (Model of Emissions of Gases and Aerosols from Nature). *Atmos. Chem. Phys.* 6, 3181-3210.
- 568 Han, H., Liu, J.E., Shu, L., Wang, T.J., Yuan, H.L., 2020. Local and synoptic meteorological influences on daily variability in
569 summertime surface ozone in eastern China. *Atmos Chem Phys* 20, 203-222.
- 570 Kerr, R.A., 1986. Chinook Winds Resemble Water Flowing over a Rock. *Science* 231, 1244-1245.
- 571 Kirchgaessner, A., King, J.C., Anderson, P.S., 2021. The Impact of Föhn Conditions Across the Antarctic Peninsula on Local
572 Meteorology Based on AWS Measurements. *Journal of Geophysical Research: Atmospheres* 126, e2020JD033748.
- 573 Li, J., Sun, Z., Lenschow, D.H., Zhou, M., Dou, Y., Cheng, Z., Wang, Y., Li, Q., 2020a. A foehn-induced haze front in Beijing:
574 observations and implications. *Atmos. Chem. Phys.* 20, 15793-15809.
- 575 Li, J., Zhang, J., Bai, M., Su, J., Li, Q., Jia, X., 2025. Identification and characterization of foehn events in Beijing and their
576 impact on air pollution episodes. *Atmos. Chem. Phys.* 25, 8683-8700.
- 577 Li, X., Xia, X., Wang, L., Cai, R., Zhao, L., Feng, Z., Ren, Q., Zhao, K., 2015. The role of foehn in the formation of heavy air
578 pollution events in Urumqi, China. *Journal of Geophysical Research: Atmospheres* 120, 5371-5384.
- 579 Li, X., Xia, X., Zhong, S., Luo, L., Yu, X., Jia, J., Zhao, K., Li, N., Liu, Y., Ren, Q., 2020b. Shallow foehn on the northern
580 leeside of Tianshan Mountains and its influence on atmospheric boundary layer over Urumqi, China — A climatological
581 study. *Atmospheric Research* 240, 104940.
- 582 Li, Y., Chen, M., Miao, S., Zhang, G., Huang, Q., Zhang, S., 2026. Evaluation of three scale-aware planetary boundary layer
583 schemes in WRF Model during Beijing 2022 Winter Olympics. *Atmospheric Research* 328, 108416.
- 584 Liao, Z., Pan, Y., Ma, P., Jia, X., Cheng, Z., Wang, Q., Dou, Y., Zhao, X., Zhang, J., Quan, J., 2023. Meteorological and
585 chemical controls on surface ozone diurnal variability in Beijing: A clustering-based perspective. *Atmospheric*

586 Environment 295, 119566.

587 Liao, Z., Sun, J., Yao, J., Liu, L., Li, H., Liu, J., Xie, J., Wu, D., Fan, S., 2018. Self-organized classification of boundary layer
588 meteorology and associated characteristics of air quality in Beijing. *Atmos. Chem. Phys.* 18, 6771-6783.

589 Liao, Z.H., Jia, X.C., Qiu, Y.L., Quan, J.N., Pan, Y.B., Ma, P.K., Cheng, Z.G., Wang, Q.Q., 2024. Synoptic controls on
590 warm-season O₃ pollution in eastern China: A focus on O₃-NO_x-VOC chemistry. *Atmospheric Research* 311, 107660.

591 Liu, J.D., Wang, L.L., Li, M.G., Liao, Z.H., Sun, Y., Song, T., Gao, W.K., Wang, Y.H., Li, Y., Ji, D.S., Hu, B., Kerminen, V.M.,
592 Wang, Y.S., Kulmala, M., 2019. Quantifying the impact of synoptic circulation patterns on ozone variability in northern
593 China from April to October 2013-2017. *Atmos Chem Phys* 19, 14477-14492.

594 Liu, S., Liang, X.-Z., 2010. Observed Diurnal Cycle Climatology of Planetary Boundary Layer Height. *Journal of Climate* 23,
595 5790-5809.

596 Luo, R., Zheng, Y., Chen, M., 2020. Mechanism of a rare night sudden intense warming event in Beijing and surrounding
597 area. *Meteorol. Monthly (in Chinese)* 46, 478-489.

598 Ma, Y., Yang, Y., Hu, X., Gan, R., 2015. Characteristics and Mechanisms of the Sudden Warming Events in the Nocturnal
599 Atmospheric Boundary Layer: A Case Study Using WRF. *Journal of Meteorological Research* 29, 747-763.

600 Miltenberger, A.K., Reynolds, S., Sprenger, M., 2016. Revisiting the latent heating contribution to foehn warming:
601 Lagrangian analysis of two foehn events over the Swiss Alps. *Quarterly Journal of the Royal Meteorological Society* 142,
602 2194-2204.

603 Ouyang, S., Deng, T., Liu, R., Chen, J., He, G., Leung, J.C.H., Wang, N., Liu, S.C., 2022. Impact of a subtropical high and a
604 typhoon on a severe ozone pollution episode in the Pearl River Delta, China. *Atmos. Chem. Phys.* 22, 10751-10767.

605 Pal, S., Lee, T.R., 2019. Advected Air Mass Reservoirs in the Downwind of Mountains and Their Roles in Overrunning
606 Boundary Layer Depths Over the Plains. *Geophysical Research Letters* 46, 10140-10149.

607 Seibert, P., Feldmann, H., Neininger, B., Bäuml, M., Trickl, T., 2000. South foehn and ozone in the Eastern Alps – case
608 study and climatological aspects. *Atmospheric Environment* 34, 1379-1394.

609 Shu, L., Xie, M., Wang, T., Gao, D., Chen, P., Han, Y., Li, S., Zhuang, B., Li, M., 2016. Integrated studies of a regional ozone
610 pollution synthetically affected by subtropical high and typhoon system in the Yangtze River Delta region, China. *Atmos.*
611 *Chem. Phys.* 16, 15801-15819.

612 Stein, A.F., Draxler, R.R., Rolph, G.D., Stunder, B.J.B., Cohen, M.D., Ngan, F., 2015. NOAA's HYSPLIT Atmospheric Transport
613 and Dispersion Modeling System. *Bulletin of the American Meteorological Society* 96, 2059-2077.

614 Steinhoff, D.F., Bromwich, D.H., Speirs, J.C., McGowan, H.A., Monaghan, A.J., 2014. Austral summer foehn winds over
615 the McMurdo dry valleys of Antarctica from Polar WRF. *Quarterly Journal of the Royal Meteorological Society* 140,
616 1825-1837.

617 Stull, R.B., 1988. *An Introduction to Boundary Layer Meteorology*; Kluwer Academic Publishers, Dordrecht, The
618 Netherlands.

619 Tang, G., Zhang, J., Zhu, X., Song, T., Münkel, C., Hu, B., Schäfer, K., Liu, Z., Zhang, J., Wang, L., Xin, J., Suppan, P., Wang, Y.,
620 2016. Mixing layer height and its implications for air pollution over Beijing, China. *Atmos. Chem. Phys.* 16, 2459-2475.

621 Wang, X.Y., Wang, K.C., 2014. Estimation of atmospheric mixing layer height from radiosonde data. *Atmos. Meas. Tech.* 7,
622 1701-1709.

623 Wu, W., Fu, T.-M., Arnold, S.R., Spracklen, D.V., Zhang, A., Tao, W., Wang, X., Hou, Y., Mo, J., Chen, J., Li, Y., Feng, X., Lin,
624 H., Huang, Z., Zheng, J., Shen, H., Zhu, L., Wang, C., Ye, J., Yang, X., 2024. Temperature-Dependent Evaporative
625 Anthropogenic VOC Emissions Significantly Exacerbate Regional Ozone Pollution. *Environmental Science & Technology*
626 58, 5430-5441.

627 Xu, J., Zhang, Z., Zhao, X., Zhang, J., 2024. Synthetically impacts of the topography and typhoon periphery on the
628 atmospheric boundary layer structure and special regional pollution pattern of O₃ in North China Plain. *Atmospheric*
629 *Environment* 330, 120566.

630 Xu, X., Shu, S., Wang, G., Li, W., 2026. Machine-learning-based identification of influencing factors and synoptic patterns
631 of foehn on the eastern foothills of the Taihang Mountains, China. *Atmos. Chem. Phys.* 26, 6507-6519.

632 Yang, X., Yang, M., Li, J., Zhang, S., 2018. Impact analysis of a Taihang Mountain foehn on haze intensity. *Meteorol.*
633 *Monthly (in Chinese)* 44, 313-319.

634 Zhang, Q., Streets, D.G., Carmichael, G.R., He, K.B., Huo, H., Kannari, A., Klimont, Z., Park, I.S., Reddy, S., Fu, J.S., Chen, D.,
635 Duan, L., Lei, Y., Wang, L.T., Yao, Z.L., 2009. Asian emissions in 2006 for the NASA INTEX-B mission. *Atmos. Chem. Phys.* 9,
636 5131-5153.

637 Zhang, S., Zeng, G., Yang, X., Wu, R., Yin, Z., 2021. Comparison of the influence of two types of cold surge on haze
638 dispersion in eastern China. *Atmos. Chem. Phys.* 21, 15185-15197.

639 Zong, L., Yang, Y., Xia, H., Yuan, J., Guo, M., 2023. Elucidating the Impacts of Various Atmospheric Ventilation Conditions
640 on Local and Transboundary Ozone Pollution Patterns: A Case Study of Beijing, China. *Journal of Geophysical Research:*
641 *Atmospheres* 128, e2023JD039141.

642